Study of a depressurisation process at low Mach number in a nuclear reactor core

Andrea Bondesan, Stéphane Dellacherie, Hélène Hivert, Jonathan Jung, Vanessa Lleras, Colin Mietka, Yohan Penel

Study of a Depressurisation Process at Low Mach number in a nuclear reactor core

Andrea Bondesan Stéphane Dellacherie Hélène Hivert Jonathan Jung
Vanessa Lleras Colin Mietka Yohan Penel

January 19, 2016

Abstract

This paper deals with the numerical treatment of two additional terms in the Lmnc-system derived and studied in previous publications and modelling the coolant in a nuclear reactor core. On the one hand, we investigate the influence of the thermal conduction upon steady analytical solutions and upon numerical strategies designed in dimensions 1 and 2. On the other hand, we consider a time-varying thermodynamic pressure that enables to simulate a larger variety of physical situations. Taking into account the resulting terms in the equations lead us to adapt numerical methods to ensure accuracy.

1 Introduction

For the purpose of studying thermodynamic and kinematic properties of the coolant fluid in the primary circuit of a pressurised water reactor (PWR), the low Mach nuclear core model (Lmnc) was introduced in [4]. As the Navier-Stokes equations modelling the behaviour of a compressible fluid raise several theoretical and numerical issues, a simplification process was applied. The incompressible model was not under consideration since it does not account for high thermal/pressure variations. That is why an intermediate system was derived by means of an asymptotic expansion with respect to the Mach number [11, 12, 14] whose order of magnitude is reportedly small in the situations of interest.

Due to the decoupling of the pressure field into thermodynamic/dynamic pressure variables, the mathematical structure of the resulting Lmnc model is easier to deal with whether it be concerning the analysis (derivation of analytical solutions in dimension 1) or the numerical simulations (coupling of robust numerical methods). The major advantage of this approach is that the thermodynamic pressure involved in the equation of state (EOS) does not depend on space variables. In this setting, it is prescribed by boundary conditions. In other cases, it can be seen as the solution of an ODE [8].

In previous works, the data was chosen so that the thermodynamic pressure is constant. In dimension 1, the authors computed transient analytical solutions without [2] and with [3] phase transition. A numerical scheme based on the method of characteristics was proposed [3]. The extension to dimension 2 was carried out in [2, 5] by means of the finite element software FreeFem++ [10] still coupled to the method of characteristics [17]. All these results were obtained modelling the thermodynamic properties of water with the Stiffened Gas EOS whose parameters are tuned separately for the liquid phase and the vapour phase. To improve the physical accuracy of the results in the range of pressures and temperatures at stake, the analytical EOS was replaced in [6] by fitting polynomials using experimental values extracted from [13].

The present work consists in enriching the model by taking into account two additional phenomena. On the one hand, we investigate the case of a time-varying thermodynamic pressure which enables to deal with more general situations like depressurisation processes for safety evaluations. This induces new terms in the equations but it does not raise additional issues in the design of the numerical scheme. The very point is that the tabulated EOS consists of polynomials whose coefficients depend on the variable thermodynamic

pressure. Hence these coefficients must be recalculated at each time step which implies extra computational time. On the other hand, we aim at pointing out the low influence of thermal diffusion effects on the overall behaviour of the fluid. The resulting additional terms in the formulation change the mathematical structure of the equation and requires substantial modifications of the numerical schemes.

More precisely, the LMNC model reads

$$\begin{cases} \nabla\cdot\boldsymbol{u} = -\dfrac{p_0'(t)}{\rho\big(h,p_0(t)\big)c^2\big(h,p_0(t)\big)} + \dfrac{\beta\big(h,p_0(t)\big)}{p_0(t)}\left[\nabla\cdot\big(\lambda\big(h,p_0(t)\big)\nabla T\big(h,p_0(t)\big)\big) + \Phi\right], & \text{(1a)} \\ \rho\big(h,p_0(t)\big)\times\left[\partial_t h + \boldsymbol{u}\cdot\nabla h\right] = \nabla\cdot\left[\lambda\big(h,p_0(t)\big)\nabla T\big(h,p_0(t)\big)\right] + \Phi + p_0'(t), & \text{(1b)} \\ \rho\big(h,p_0(t)\big)\times\left[\partial_t\boldsymbol{u} + (\boldsymbol{u}\cdot\nabla)\boldsymbol{u}\right] - \nabla\cdot\sigma(\boldsymbol{u}) + \nabla\bar{p} = \rho\big(h,p_0(t)\big)\boldsymbol{g}, & \text{(1c)} \end{cases}$$

for $(t,\boldsymbol{x})\in\mathbb{R}^+\times\Omega_d$.[1]

The unknowns are the enthalpy h, the velocity field $\boldsymbol{u}$ and the dynamic pressure $\bar{p}$. Data are the thermodynamic pressure $t\mapsto p_0(t)$, the power density of the core $(t,\boldsymbol{x})\mapsto\Phi(t,\boldsymbol{x})$ and the gravity field $\boldsymbol{g}$. The Cauchy stress tensor σ is classically expressed involving the Lamé viscosity coefficients. Other variables such as density ρ, speed of sound c, compressibility coefficient $\beta\overset{\text{def}}{=}-\frac{p}{\rho^2}\frac{\partial\rho}{\partial h}$, thermal conductivity λ or temperature T are computed by means of the EOS or constitutive laws as functions of h and p_0 with separate expressions depending on the phases (liquid, mixture, gas). The reader is referred to [6] for more details about the modelling of the mixture phase and the computation of variables at saturation. Our modelling is enthalpy-oriented: the values of the enthalpy determine the related phase and all thermodynamic variables are deduced from h. Denoting by $p\mapsto h_{\mathfrak{l}}^s(p)$ and $p\mapsto h_{\mathfrak{g}}^s(p)$ the enthalpies at saturation in the liquid and in the vapour, we have

$$\zeta(h,p) = \begin{cases} \zeta_{\mathfrak{l}}(h,p), & \text{if } h\le h_{\mathfrak{l}}^s(p), \\ \zeta_{\mathfrak{m}}(h,p), & \text{if } h_{\mathfrak{l}}^s(p)<h<h_{\mathfrak{g}}^s(p), \\ \zeta_{\mathfrak{g}}(h,p), & \text{if } h\ge h_{\mathfrak{g}}^s(p), \end{cases}$$

for $\zeta\in\{\rho,\beta,\lambda,T,c\}$. $\zeta_{\mathfrak{l}}$ and $\zeta_{\mathfrak{g}}$ are expressions of EOS or constitutive laws in the liquid and vapour phases. $\zeta_{\mathfrak{m}}$ comes from modelling choices (see [6]).

For practical reasons, we do not use the EOS to express T in System (1) but we rather apply thermodynamic principles that state

$$\lambda(h,p)\nabla T(h,p) = \Lambda(h,p)\nabla h, \quad \text{with} \quad \Lambda(h,p) = \begin{cases} \Lambda_{\mathfrak{l}}(h,p)\overset{\text{def}}{=}\dfrac{\lambda_{\mathfrak{l}}(h,p)}{c_{p_{\mathfrak{l}}}(h,p)}, & \text{if } h\le h_{\mathfrak{l}}^s(p), \\ \Lambda_{\mathfrak{m}}(h,p)\equiv 0, & \text{if } h_{\mathfrak{l}}^s(p)<h<h_{\mathfrak{g}}^s(p), \\ \Lambda_{\mathfrak{g}}(h,p)\overset{\text{def}}{=}\dfrac{\lambda_{\mathfrak{g}}(h,p)}{c_{p_{\mathfrak{g}}}(h,p)}, & \text{if } h\ge h_{\mathfrak{g}}^s(p), \end{cases} \qquad (2)$$

where c_p is the heat capacity at constant pressure. The value in the mixture is set to 0 as the temperature is constant within the saturation dome.

As our goal is here to derive relevant numerical methods and to assess them, the sequel is restricted to the Stiffened Gas law for the sake of clarity. Indeed, it is then possible to exhibit analytical steady solutions (Prop. 1) which will be compared to numerical solutions. It can be then applied to tabulated laws without restriction.

[1] $\Omega_1=[0,L_y]$ and $\Omega_2=[0,L_x]\times[0,L_y]$.

The Stiffened Gas law [3] reads

	$\beta(h,p)$	$q(h,p)$	$T(h,p)$	$\Lambda(h,p)$
$h \le h_{\mathfrak{l}}^s(p)$	$\dfrac{\gamma_{\mathfrak{l}}-1}{\gamma_{\mathfrak{l}}}\dfrac{p}{p+\pi_{\mathfrak{l}}}$	$q_{\mathfrak{l}}$	$\dfrac{h-q_{\mathfrak{l}}}{c_{p_{\mathfrak{l}}}}$	$\dfrac{\lambda_{\mathfrak{l}}}{c_{p_{\mathfrak{l}}}}$
$h_{\mathfrak{l}}^s(p) < h < h_{\mathfrak{g}}^s(p)$	$p\cdot\dfrac{\frac{1}{\rho_{\mathfrak{g}}^s}-\frac{1}{\rho_{\mathfrak{l}}^s}}{h_{\mathfrak{g}}^s-h_{\mathfrak{l}}^s}(p)$	$\dfrac{\rho_{\mathfrak{g}}^s h_{\mathfrak{g}}^s-\rho_{\mathfrak{l}}^s h_{\mathfrak{l}}^s}{\rho_{\mathfrak{g}}^s-\rho_{\mathfrak{l}}^s}(p)$	$T^s(p)$	0
$h \ge h_{\mathfrak{g}}^s(p)$	$\dfrac{\gamma_{\mathfrak{g}}-1}{\gamma_{\mathfrak{g}}}\dfrac{p}{p+\pi_{\mathfrak{g}}}$	$q_{\mathfrak{g}}$	$\dfrac{h-q_{\mathfrak{g}}}{c_{p_{\mathfrak{g}}}}$	$\dfrac{\lambda_{\mathfrak{g}}}{c_{p_{\mathfrak{g}}}}$

The density is given by

$$\rho(h,p) = \frac{p/\beta(h,p)}{h-q(h,p)}. \tag{3}$$

Values of parameters γ_κ, π_κ, q_κ and c_{p_κ}, $\kappa \in \{\mathfrak{l},\mathfrak{g}\}$, for $p_0 = 155\,\text{bar}$ are given in [3, Table 1]. The expression of the speed of sound can be found in [3, Appendix B].

When no thermal diffusion is involved, the problem is hyperbolic with respect to h. The diffusion term turns the problem parabolic and requires additional boundary conditions. We then impose

Location	Enthalpy	Velocity/pressure
Bottom ($y=0$)	$h = h_e$	$\rho(h_e,p_0)\boldsymbol{u} = (0, D_e)$
Lateral ($x \in \{0, L_x\}$)	$\Lambda(h,p_0)\nabla h\cdot\boldsymbol{n} = 0$	$\boldsymbol{u}\cdot\boldsymbol{n} = 0$ $\sigma(\boldsymbol{u})\boldsymbol{n}\cdot\boldsymbol{\tau} = 0$
Top ($y = L_y$)	$\Lambda(h,p_0)\nabla h\cdot\boldsymbol{n} = 0$	$\sigma(\boldsymbol{u})\boldsymbol{n} - \bar{p}\boldsymbol{n} = \boldsymbol{0}$

Notice that when Λ vanishes, no condition is then imposed upon h and the model is compatible with the degeneracy of the thermal conductivity.

As for initial conditions, we impose $h(0,\boldsymbol{x}) = h_0(\boldsymbol{x})$, $\boldsymbol{u}(0,\boldsymbol{x}) = \boldsymbol{u}_0(\boldsymbol{x})$ and $\bar{p}(0,\boldsymbol{x}) = 0$.

We finally assume:

- The input rate D_e is non-negative;
- The thermodynamic pressure p_0 remains non-negative;
- h_e is such that ρ_e computed thanks to (3) exists and is positive; moreover, h_e corresponds to a liquid phase;
- Initial data $(h_0, \boldsymbol{u}_0, p_0)$ are well prepared, *i.e.* they satisfy Equation (1a).

2 Study of the 1-dimensional case

In dimension 1, the system has a particular structure as the momentum equation (1c) decouples from the others. Hence in this section we only focus on the subsystem

$$\begin{cases} \partial_y v = -\dfrac{p_0'(t)}{\rho\big(h,p_0(t)\big)c^2\big(h,p_0(t)\big)} + \dfrac{\beta\big(h,p_0(t)\big)}{p_0(t)}\left[\partial_y\big(\Lambda\big(h,p_0(t)\big)\partial_y h\big) + \Phi\right], & \text{(4a)} \\ \rho\big(h,p_0(t)\big)\times\left[\partial_t h + v\cdot\partial_y h\right] = \partial_y\left[\Lambda\big(h,p_0(t)\big)\partial_y h\right] + \Phi + p_0'(t). & \text{(4b)} \end{cases}$$

The dynamic pressure $\bar{p}$ is then recovered by a direct integration of (1c). When $\Lambda \equiv 0$, using the Stiffened Gas law implies that β is piecewise constant and (4a) decouples from (4b): This no longer holds as soon as one uses another EOS or when $\Lambda \neq 0$.

2.1 Steady solutions

Transient 1D solutions can be found in [3, 9] for constant p_0 and $\lambda = 0$, and in [16] for perfect gas, time-varying p_0 and $\lambda = 0$. When such solutions cannot be achieved, one tries to obtain steady solutions in order to have explicit elements to assess numerical methods. In the steady case, it comes down to focusing on the influence of thermal conduction as p_0 is necessarily a constant.

For the sake of simplicity, we assume that the power density is constant to $\Phi_0 > 0$ and we set

$$\mathcal{H}(z) = h_\mathfrak{l}^s - h_e - \frac{\Phi_0}{D_e} z + \frac{\Phi_0 \kappa_\mathfrak{l}}{D_e} \left(1 - e^{-z/\kappa_\mathfrak{l}}\right), \qquad \text{where } \kappa_\mathfrak{l} \stackrel{\text{def}}{=} \frac{\Lambda_\mathfrak{l}}{D_e}.$$

$\mathcal{H}$ is monotone-decreasing and by assumption, $\mathcal{H}(0) > 0$.

It is possible to provide a continuous steady solution of the problem as long as no vapour appears:

Proposition 1.

(a) If $\mathcal{H}(L_y) > 0$, there exists a unique steady solution corresponding to a pure liquid configuration and given by

$$h_\infty(y) = h_e + \frac{\Phi_0}{D_e} y - \frac{\Phi_0 \kappa_\mathfrak{l}}{D_e} e^{-L_y/\kappa_\mathfrak{l}} \left(e^{y/\kappa_\mathfrak{l}} - 1\right).$$

(b) Let us assume that $\mathcal{H}(L_y) \leq 0$ and that $\mathcal{H}(L_y) > \frac{\Phi_0 \kappa_\mathfrak{l}}{D_e} \left(e^{-y_\mathfrak{l}^s/\kappa_\mathfrak{l}} - e^{-L_y/\kappa_\mathfrak{l}}\right) - (h_\mathfrak{g}^s - h_\mathfrak{l}^s)$ where $y_\mathfrak{l}^s$ is the unique solution in $[0, L_y]$ of $\mathcal{H}(y_\mathfrak{l}^s) = 0$. Then there exists a unique continuous steady solution corresponding to a liquid-mixture configuration and given by

$$h_\infty(y) = \begin{cases} h_e + \dfrac{\Phi_0}{D_e} y - \dfrac{\Phi_0 \kappa_\mathfrak{l}}{D_e} e^{-y_\mathfrak{l}^s/\kappa_\mathfrak{l}} \left(e^{y/\kappa_\mathfrak{l}} - 1\right), & \text{if } y \in (0, y_\mathfrak{l}^s), \\ h_\mathfrak{l}^s + \dfrac{\Phi_0}{D_e}(y - y_\mathfrak{l}^s), & \text{if } y \in (y_\mathfrak{l}^s, L_y). \end{cases}$$

Proof. Let us first remark that combining the steady counterparts of (4a-4b) leads to $\partial_y(\rho v) = 0$.[2] Hence $\rho v = D_e$.

(a) Assume that only liquid is present in the steady state. Then Equation (4b) reads

$$\partial_{yy}^2 h - \frac{1}{\kappa_\mathfrak{l}} \partial_y h = -\frac{\Phi_0}{D_e \kappa_\mathfrak{l}}. \tag{5}$$

Solving this 1st-order ODE for $\partial_y h$ and applying the boundary condition on the top yields

$$\partial_y h(y) = \frac{\Phi_0}{D_e} \left(1 - e^{(y - L_y)/\kappa_\mathfrak{l}}\right).$$

We deduce that h is monotone-increasing as well as the expression given in Prop. 1(a). The preliminary assumption (reactor filled with liquid) is valid as long as $h(L_y) < h_\mathfrak{l}^s$ which is equivalent to $\mathcal{H}(L_y) > 0$.

(b) If $\mathcal{H}(L_y) \leq 0$, there cannot only be liquid in the core. We are thus looking for a weak solution of the steady Lmnc model which corresponds to a liquid phase over $(0, y_\mathfrak{l}^s)$ (for some $y_\mathfrak{l}^s$ to be determined) and to a mixture phase over $(y_\mathfrak{l}^s, L_y)$. The conservative steady version of Equation (4b) is

$$\partial_y\big(\rho(h, p_0) h v\big) = \partial_y\big[\Lambda(h, p_0) \partial_y h\big] + \Phi. \tag{6}$$

[2] We recall that $\beta \stackrel{\text{def}}{=} -\frac{p}{\rho^2} \frac{\partial \rho}{\partial h}$.

The weak formulation associated to the previous equality is

$$\forall\, \varphi \in \mathcal{D}\big((0,L_y)\big),\ \int_0^{L_y} [\rho(h,p_0)hv\partial_y\varphi + \varphi\Phi - \Lambda(h,p_0)\partial_y h\partial_y\varphi]\,\mathrm{d}y = 0.$$

If we take some $\varphi \in \mathcal{D}\big((y_-,y_+)\big)$ with $0 < y_- < y_\mathfrak{l}^s < y_+ < L_y$, as the solutions on both sides of $y_\mathfrak{l}^s$ are smooth, we can split the integral in two parts over $(y_-,y_\mathfrak{l}^s)$ and $(y_\mathfrak{l}^s,y_+)$ and integrate by parts:

$$\begin{aligned}0 = {}& \big[\rho(h,p_0)hv\varphi\big]_{y_-}^{y_\mathfrak{l}^s} + \big[\rho(h,p_0)hv\varphi\big]_{y_\mathfrak{l}^s}^{y_+} - \big[\Lambda(h,p_0)\varphi\partial_y h\big]_{y_-}^{y_\mathfrak{l}^s} \\ & - \int_{y_-}^{y_\mathfrak{l}^s} \varphi \underbrace{\big[\partial_y\big(\rho(h,p_0)hv\big) - \varphi\Phi - \varphi\partial_y\big(\Lambda(h,p_0)\partial_y h\big)\big]}_{=0 \text{ by (6)}}\,\mathrm{d}y - \int_{y_\mathfrak{l}^s}^{y_+} \varphi \underbrace{\big[\partial_y\big(\rho(h,p_0)hv\big) - \varphi\Phi\big]}_{=0 \text{ by (6)},\ \Lambda_\mathfrak{m}=0}\,\mathrm{d}y.\end{aligned}$$

We deduce that

$$(\Lambda(h,p_0)\partial_y h)_{y_\mathfrak{l}^{s-}} + D_e\,[\![h]\!]_{y_\mathfrak{l}^s} = 0.$$

To obtain a continuous solution ($[\![h]\!]_{y_\mathfrak{l}^s} = 0$), we thus take

$$(\Lambda(h,p_0)\partial_y h)_{y_\mathfrak{l}^{s-}} = 0. \tag{7}$$

Notice that the continuity of h at $y = y_\mathfrak{l}^s$ implies the continuity of $\rho(h,p_0)$ and then the continuity of $v = De/\rho(h,p_0)$.

We integrate ODE (5) over $(0,y_\mathfrak{l}^s)$ taking boundary condition (7) into account. This leads to

$$h(y) = h_e + \frac{\Phi_0}{D_e}\left(y - \kappa_\mathfrak{l} e^{-y_\mathfrak{l}^s/\kappa_\mathfrak{l}}(e^{y/\kappa_\mathfrak{l}} - 1)\right).$$

$y_\mathfrak{l}^s$ is determined by solving the equation $h(y_\mathfrak{l}^s) = h_\mathfrak{l}^s$ which is equivalent to $\mathcal{H}(y_\mathfrak{l}^s) = 0$, whose root is unique. As for the domain $(y_\mathfrak{l}^s, L_y)$, we trivially obtain the expression for h as $\Lambda_\mathfrak{m} = 0$. This holds as long as $h_\mathfrak{g}^s$ is not reached. If so, it is necessary at the boundary $y = L_y$ first. The restriction thus reads $h(L_y) = h_\mathfrak{l}^s + \frac{\Phi_0}{D_e}(L_y - y_\mathfrak{l}^s) < h_\mathfrak{g}^s$ which can be turned into the equivalent inequality in terms of $\mathcal{H}$ given in the statement of Prop. 1(b). □

Remark. *Appearance of vapour raises many issues as discontinuities apparently occur. This will be investigated in future works.*

2.2 Numerical scheme

The numerical strategy implemented in the present work consists in adapting the numerical method of characteristics (MOC) designed in [3, 15] to decouple the two equations in (4). As the MOC scheme is unconditionally stable, the point is here to take into account the diffusion term in Equation (4b) without imposing a restrictive (parabolic) stability condition. That is why an implicit version is considered. Equation (4a) is directly integrated in a second step.

We consider a homogeneous cartesian grid $(y_i = i\Delta y)_{0\le i\le N_y}$ where $\Delta y = \frac{L_y}{N_y}$ for some integer $N_y \ge 1$ and a uniform time discretisation $(t^n = n\Delta t)_{n\ge 0}$ for some time step $\Delta t > 0$.

More precisely, to solve Equation (4b), we introduce the characteristic field $\tau \mapsto \chi(\tau; t^{n+1}, y_i)$ as the solution of the ODE

$$\begin{cases} \dfrac{\mathrm{d}}{\mathrm{d}\tau}\chi(\tau;t^{n+1},y_i) = v\big(\tau,\chi(\tau;t^{n+1},y_i)\big), \quad \tau \le t^{n+1}, \\ \chi(t^{n+1};t^{n+1},y_i) = y_i, \end{cases} \tag{8}$$

so that Equation (4b) reads

$$\frac{\mathrm{d}}{\mathrm{d}\tau}h\big(\tau,\chi(\tau;t^{n+1},y_i)\big) = \frac{p_0'(\tau) + \Phi\big(\tau,\chi(\tau;t^{n+1},y_i)\big)}{\rho\big(h\big(\tau,\chi(\tau;t^{n+1},y_i)\big),p_0(\tau)\big)} + \left[\frac{\partial_y\big(\Lambda(h,p_0)\partial_y h\big)}{\rho(h,p_0)}\right]\big(\tau,\chi(\tau;t^{n+1},y_i)\big). \tag{9}$$

Given the numerical solution (h_i^n, v_i^n) at time t^n, Equation (8) can be solved numerically at 1st or 2nd order [15] so as to compute the numerical foot of the characteristic curve defined by

$$\xi_i^n \approx \chi(t^n; t^{n+1}, y_i). \tag{10}$$

As ξ_i^n may not be located at a mesh node, an interpolation process is required to approximate $h(t^n, \xi_i^n)$. A procedure ensuring the maximum principle at order 3 is described in [3]. Denoting by $\hat{h}_i^n$ this interpolated value, the left hand side in (9) is approximated by a finite difference so that a discrete formulation of Equation (4b) is

$$\frac{h_i^{n+1} - \hat{h}_i^n}{\Delta t} = \frac{p_0'(t^n) + \Phi(t^n, \xi_i^n) + \left[\partial_y \left(\Lambda\big(h^n, p_0(t^n)\big)\partial_y h^{n+1}\right)\right]_{y_i}}{\rho\big(\hat{h}_i^n, p_0(t^n)\big)},$$

The diffusion term is implicited but the conductivity is linearised as set to time t^n. It is discretised by means of a 3-point finite difference

$$\begin{aligned}\left[\partial_y \left(\Lambda\big(h^n, p_0(t^n)\big)\partial_y h^{n+1}\right)\right]_{y_i} &= \frac{\Lambda\big(h_{i+1/2}^n, p_0(t^n)\big)(\partial_y h^{n+1})_{i+1/2} - \Lambda\big(h_{i-1/2}^n, p_0(t^n)\big)(\partial_y h^{n+1})_{i-1/2}}{\Delta y} \\ &= \frac{\Lambda\big(h_{i+1/2}^n, p_0(t^n)\big)\left(h_{i+1}^{n+1} - h_i^{n+1}\right)}{\Delta y^2} - \frac{\Lambda\big(h_{i-1/2}^n, p_0(t^n)\big)\left(h_i^{n+1} - h_{i-1}^{n+1}\right)}{\Delta y^2}.\end{aligned}$$

The intermediate conductivity $\Lambda\big(h_{i+1/2}^n, p_0(t^n)\big)$ is computed as the harmonic mean of $\Lambda\big(h_i^n, p_0(t^n)\big)$ and $\Lambda\big(h_{i+1}^n, p_0(t^n)\big)$.

Close to the boundary, a special treatment must be done as the characteristic curve arising from (t^{n+1}, y_i) may cross the boundary between t^n and t^{n+1} (see [15] for more details).

The resulting implicit numerical scheme yields a tridiagonal linear system which can be solved without matrix inversion by means of the Thomas algorithm [1].

A restriction upon the time step must be imposed to ensure a good level of accuracy (and not for stability issues), either by a standard CFL condition $\Delta t \leq \Delta y / \max_i |v_i^n|$ or by a threshold.

As for the integration of the divergence constraint (4a) to recover the velocity field, a particular attention must be paid to avoid instabilities due to the discontinuity of β and c^2. In cells (y_{i-1}, y_i) where phase transition occurs, *i.e.* when $(h_\mathfrak{l}^s - h_{i-1}^{n+1})(h_i^{n+1} - h_\mathfrak{l}^s) > 0$ or $(h_\mathfrak{g}^s - h_{i-1}^{n+1})(h_i^{n+1} - h_\mathfrak{g}^s) > 0$,[3] the integral must be split into two parts: one over (y_{i-1}, y_*^{n+1}) using liquid parameters and one over (y_*^{n+1}, y_i) using mixture parameters, where $(y_*^{n+1}, h_\mathfrak{l}^s)$ is a linear approximation of the function passing through (y_{i-1}, h_{i-1}^{n+1}) and (y_i, h_i^{n+1}).

In the sequel, the adapted MOC scheme is called "MOC-d" scheme.

2.3 Simulations

Unless specified, the data are set as follows in the numerical simulations:

h_e is computed by inverting the EOS (3), namely

$$h_e = q_\mathfrak{l} + \frac{\gamma_\mathfrak{l} - 1}{\gamma_\mathfrak{l}} \frac{\rho_e}{p_0 + \pi_\mathfrak{l}} \approx 1.191\,726 \times 10^6\,\mathrm{J \cdot K^{-1}}.$$

We recall that parameters of the Stiffened Gas law for this value of p_0 can be found in [3, Appendix B], as well as enthalpies at saturation ($h_\mathfrak{l}^s = 1.627 \times 10^6\,\mathrm{J \cdot K^{-1}}$ and $h_\mathfrak{g}^s = 3.004 \times 10^6\,\mathrm{J \cdot K^{-1}}$).

The following simulations are not related to physical configurations (except § 2.3.3 and § 2.3.5-β) and are run in order to assess the modified algorithm and the model itself. Comparisons to the steady state from

[3] We do not present cases where vapour appears as we lack theoretical information. The algorithm is however implemented to handle all phases.

L_y	Length of the core	$4.2\,\mathrm{m}$
N_y	Number of spatial nodes	100
Δt	Time step	$0.01\,\mathrm{s}$

(a) Discretisation parameters

p_0	Thermodynamic pressure	$155 \times 10^5\,\mathrm{Pa}$ (constant)
Φ	Power density	$170 \times 10^6\,\mathrm{W \cdot m^{-3}}$ (constant)
ρ_e	Input density	$750\,\mathrm{kg \cdot m^{-3}}$ (constant)
v_e	Input velocity	$1\,\mathrm{m \cdot s^{-1}}$ (constant)
h_0	Initial enthalpy	h_e (constant)
v_0	Initial velocity	$v_e + \frac{\beta(h_0,p_0)}{p_0}\Phi y$

(b) Physical parameters

Table 1: Parameters for 1D simulations

Prop. 1, compatibility with the non-diffusive case and assessment of the robustness of the algorithm are made. Cases 2.3.1 to 2.3.4 are set with p_0 constant in order to focus on the conductivity. The reader is reminded of the fact that only the Stiffened Gas EOS is used in the present paper as the extension to tabulated laws does not raise difficulties.

2.3.1 Convergence for $\lambda \to 0$

Let us first investigate the case of a constant conductivity $\lambda_\mathfrak{l} = \lambda_\mathfrak{g} = \lambda \to 0$. The purpose is to determine whether the model for non-zero small conductivities is close to the non-diffusive model studied in previous articles. We thus compare the numerical results obtained by means of the MOC-d scheme to simulations of the Lmnc-model for $\lambda = 0$ by means of the INTMOC scheme designed in [3] and proven to be convergent. The L^2-norm pictured on Fig. 1 shows that both solutions converge to the same limit as λ goes to 0.

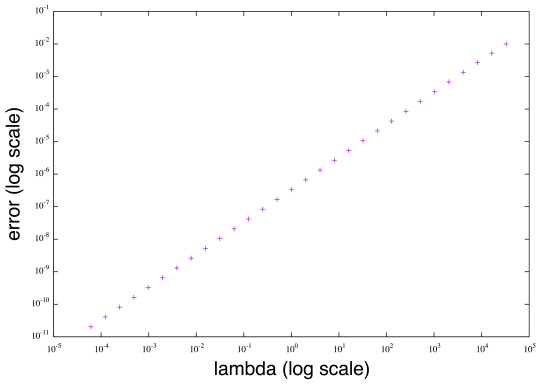

Figure 1: Case 2.3.1: Convergence for the enthalpy to the non-diffusive case in L^2-norm

2.3.2 Influence of high conductivities

Keeping a constant conductivity in both liquid and gas, we increase the corresponding value ($\lambda_\mathfrak{l} = \lambda_\mathfrak{g} = 10^6$) in order to highlight the discrepancy between non-diffusive and diffusive cases. Unlike the following example where both solutions match, we observe distinct numerical asymptotic solutions. In the mixture where

$\Lambda = 0$, both solutions are parallel straight lines. It is in the liquid phase that they have different shapes (Fig. 2(a)).

We recover the steady solution from Prop. 1 which is an exponential-like curve. Figure 2(b) shows that the numerical solution converges to the steady solution. The L^2-error is bounded from below by 10^{-2} which corresponds to the discretisation error ($\Delta y \approx 10^{-2}$).

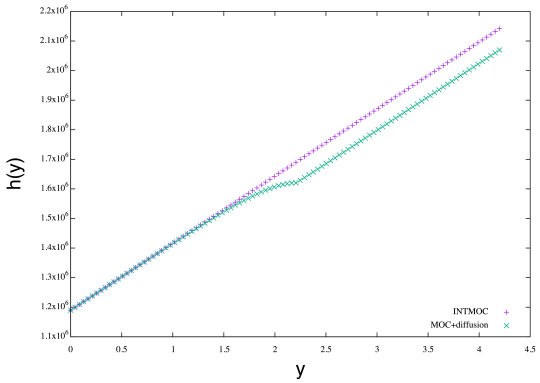

(a) Numerical solutions (enthalpy) at time 25 s

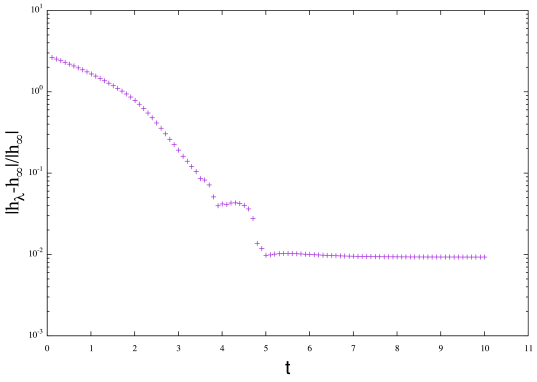

(b) Convergence to the steady state of Prop. 1

Figure 2: Case 2.3.2: Comparison between numerical solutions with and without thermal diffusion for unphysically high thermal conductivities when an asymptotic state is reached

2.3.3 Thermal conductivity in physical situations

We then run the algorithm to a configuration with physical orders of magnitude for the thermal conductivity in liquid ($\lambda_{\mathfrak{l}} = 0.5$) and vapour ($\lambda_{\mathfrak{g}} = 0.1$). According to Fig. 1, the error with the non-diffusive case is of order 10^{-6} which is confirmed by next figures.

Figures 3 show the results at time 25 s where a numerical asymptotic state is reached. We deduce from Fig. 3(a) that this state is made of liquid and mixture. The pointwise error is of order 10^{-4} and is larger in the mixture phase. This can be explained by the fact that Λ vanishes in the mixture and the MOC-d scheme degenerates to the standard MOC scheme which turns out to be less accurate than the INTMOC scheme (see [3, § 5.1]).

Hence the thermal conductivity does not play a major role for physical values which tends to legitimate not to take it into account in future works.

2.3.4 Robustness

We then consider a variable power density

$$\Phi(t,y) = \begin{cases} 600 \times 10^6\,\mathrm{W}\cdot\mathrm{m}^{-3}, & \text{if } 0 \le y \le 1.6, \\ 0\,\mathrm{W}\cdot\mathrm{m}^{-3}, & \text{if } 1.6 < y < 1.8, \\ -400 \times 10^6\,\mathrm{W}\cdot\mathrm{m}^{-3}, & \text{if } 1.6 \le y \le L. \end{cases}$$

to assess the robustness of the diffusive algorithm. Conductivities are set as in § 2.3.3. A positive power density makes the enthalpy increase (some mixture appears) while a negative one cools the flow. This is what the algorithm yields as seen on Figures 4. It manages to handle phase transition liquid to mixture (as previously) as well as mixture to liquid.

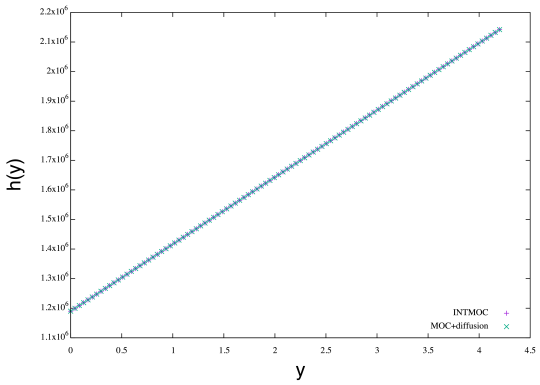

(a) Numerical solutions (enthalpy) at time 25 s

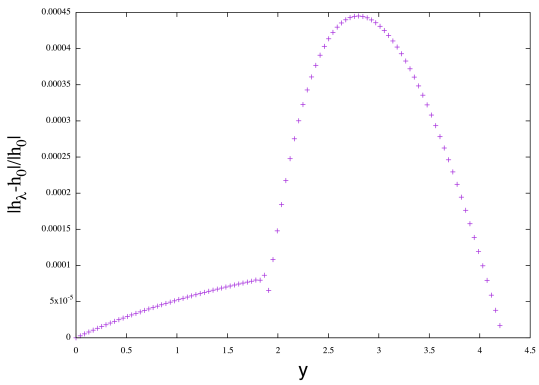

(b) Pointwise relative error (enthalpy) at time 25 s

Figure 3: Case 2.3.3: Comparison between numerical solutions with and without thermal diffusion in standard conditions when an asymptotic state is reached

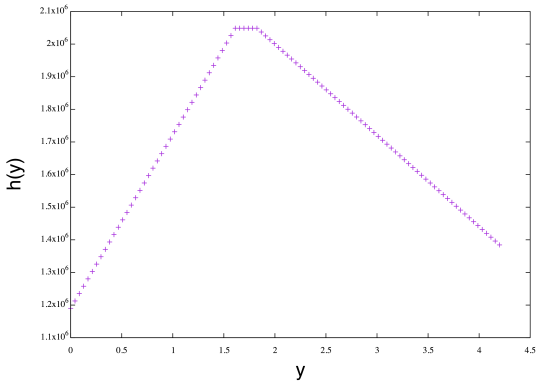

(a) Numerical enthalpy at time 25 s

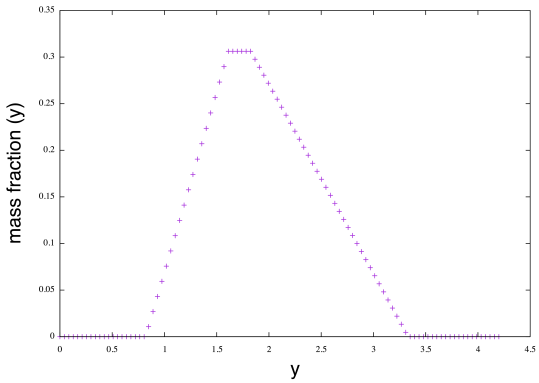

(b) Numerical mass fraction at time 25 s

Figure 4: Case 2.3.4: Profile of the numerical solution for a piecewise constant power density

2.3.5 Depressurisation processes

As simulations tend to prove the low influence of the conductivity, we take $\lambda_\ell = \lambda_g = 0$ and we focus on the effects of variable pressures. Two cases are considered: α concerns a toy-case (linear depressurisation to 40% to the initial pressure, Fig. 5(a)) to validate the algorithm whereas β corresponds to physical data of a failure of the pressuriser (Fig. 5(b)).

In case α, the depressurisation occurs once the asymptotic state is reached in initial conditions. Figures shows that the lower the thermodynamic pressure p_0, the lower the temperature at saturation T^s which can be noticed as the plateau goes down as time goes on (Fig. 5(c)). Simultaneously, the rate of mixture increases (Fig. 5(e)) which can be accounted for by the fact that the enthalpy at saturation in the liquid phase h_ℓ^s decreases as p_0 does. The profile of the temperature in the liquid is the same as the steady state for $\lambda \equiv 0$ does not depend on data at saturation nor on the EOS (see [3, Rem. 4.5] and [6, Prop. 5.1]).

In case β, the depressurisation occurs at time 1 s while the asymptotic state is not yet reached (no mixture has appeared – Fig. 5(f)). That is why we observe the plateau going up then down (Fig. 5(d)). After some seconds, an asymptotic state is reached where most of the core is under mixture phase.

As for the computational time, the variations of thermodynamic pressure require to compute data at saturation (T^s, h_ℓ^s, h_g^s) at each time step. When using the Stiffened Gas law, it has no impact compared to the constant case. However, with tabulated EOS, each fitting polynomial of thermodynamic variables (density, temperature, compressibility coefficient, ...) must be recalculated at each time step. This would

have a significant computational time but much less important than for classical compressible models where polynomials are also different at each space node.

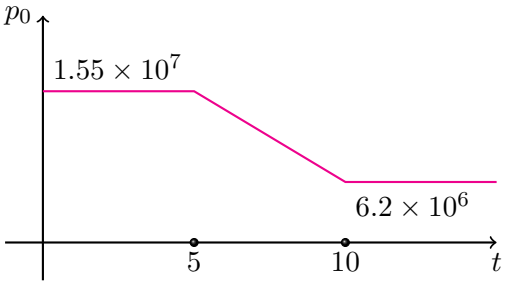

(a) Case α: profile of the depressurisation (linear decrease)

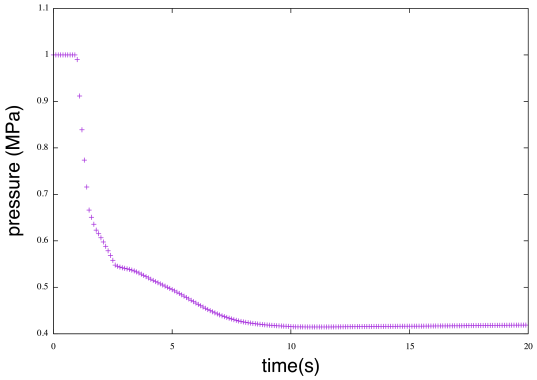

(b) Case β: profile of the depressurisation (real case)

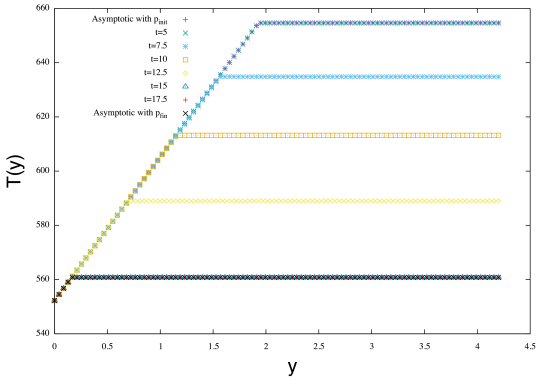

(c) Case α: Temperature at different times

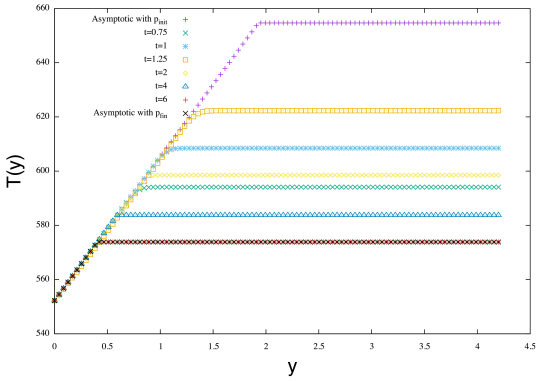

(d) Case β: Temperature at different times

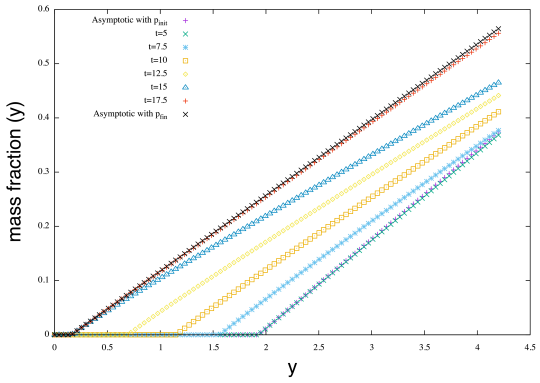

(e) Case α: Mass fraction at different times

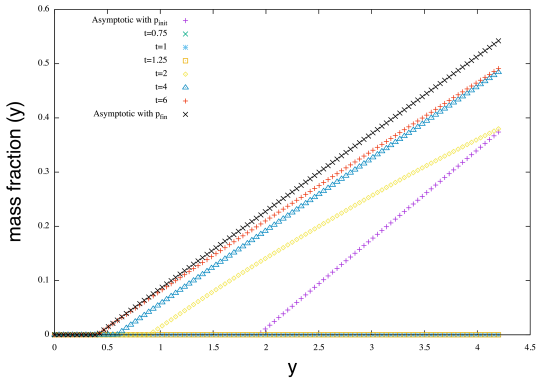

(f) Case β: Mass fraction at different times

Figure 5: Case 2.3.5: Simulations of two depressurisation processes

3 Numerical approach in dimension 2

3.1 Weak formulation

We now turn to the adaptation of the numerical scheme designed in [5] for $2D$ flows when taking into account thermal diffusion and depressurisation processes. The original algorithm is a 1st order Lagrange finite element (FE) scheme coupled to the method of characteristics integrated in the FE software FreeFem++. Due to the discontinuities of some variables involved in the model (Λ, β, c^2, ...), we decided to apply the

Discontinuous Galerkin method also implemented in FreeFem++. Well-suited to this kind of solutions, the fact still remains it induces a significant rise of the computational time as unknowns are located on vertices and edges.

We mention that the Cauchy stress tensor is given by

$$\sigma(\boldsymbol{u}) = \mu_0 \left[\big(\nabla \boldsymbol{u} + (\nabla \boldsymbol{u})^T\big) - \frac{2}{3}(\nabla \cdot \boldsymbol{u})\mathbb{I} \right]$$

where μ_0 is a constant dynamic viscosity.

The domain is $\Omega_2 = [0, L_x] \times [0, L_y]$ which is tesselated with triangles $(T_k)_{1 \leq k \leq K}$. The set of all edges is denoted by $\mathcal{E}_K$.

The weak formulation reads: "Find $(h, \boldsymbol{u}, \bar{p}) \in (h_e + \mathrm{H}) \times (\boldsymbol{u}_e + \mathrm{U}) \times \mathrm{L}^2$ such that for all $(\tilde{h}, \tilde{\boldsymbol{u}}, \tilde{p}) \in \mathrm{H} \times \mathrm{U} \times \mathrm{L}^2$

$$\begin{aligned}
\iint_{\Omega_2} (\nabla \cdot \boldsymbol{u}) \tilde{p} \, \mathrm{d}\boldsymbol{x} = \iint_{\Omega_2} \left(\frac{\beta\big(h^n, p_0(t^n)\big)\Phi}{p_0(t^n)} - \frac{p_0'(t^n)}{\rho\big(h^n, p_0(t^n)\big) c^2\big(h^n, p_0(t^n)\big)} \right) \tilde{p} \, \mathrm{d}\boldsymbol{x} \\
- \iint_{\Omega_2} \frac{\beta\big(h^n, p_0(t^n)\big)\Lambda\big(h^n, p_0(t^n)\big)}{p_0(t^n)} \nabla h^{n+1} \cdot \nabla \tilde{p} \, \mathrm{d}\boldsymbol{x} \\
+ \int_{\mathcal{E}_K} \left[\!\!\left[\frac{\beta\big(h^n, p_0(t^n)\big)\Lambda\big(h^n, p_0(t^n)\big)}{p_0(t^n)} (\nabla h^{n+1} \cdot \boldsymbol{n}_K) \tilde{p} \right]\!\!\right] \mathrm{d}\varsigma, \quad (11a)
\end{aligned}$$

$$\begin{aligned}
\iint_{\Omega_2} \rho\big(h^n, p_0(t^n)\big) \frac{h^{n+1} - h^n(\boldsymbol{\xi}^n)}{\Delta t} \tilde{h} \, \mathrm{d}\boldsymbol{x} = \\
\iint_{\Omega_2} \big(\Phi + p_0'(t^n)\big) \tilde{h} \, \mathrm{d}\boldsymbol{x} - \iint_{\Omega_2} \Lambda\big(h^n, p_0(t^n)\big) \nabla h^{n+1} \cdot \nabla \tilde{h} \, \mathrm{d}\boldsymbol{x} \\
+ \int_{\mathcal{E}_K} \left[\!\!\left[\Lambda\big(h^n, p_0(t^n)\big) (\nabla h^{n+1} \cdot \boldsymbol{n}_K) \tilde{h} \right]\!\!\right] \mathrm{d}\varsigma, \quad (11b)
\end{aligned}$$

$$\begin{aligned}
\iint_{\Omega_2} \rho\big(h^n, p_0(t^n)\big) \frac{\boldsymbol{u}^{n+1} - \boldsymbol{u}^n(\boldsymbol{\xi}^n)}{\Delta t} \cdot \tilde{\boldsymbol{u}} \, \mathrm{d}\boldsymbol{x} = \\
- \frac{\mu_0}{2} \iint_{\Omega_2} \big(\nabla \boldsymbol{u} + (\nabla \boldsymbol{u})^T\big) :: \big(\nabla \tilde{\boldsymbol{u}} + (\nabla \tilde{\boldsymbol{u}})^T\big) \, \mathrm{d}\boldsymbol{x} + \eta_0 \iint_{\Omega_2} (\nabla \cdot \boldsymbol{u})(\nabla \cdot \tilde{\boldsymbol{u}}) \, \mathrm{d}\boldsymbol{x} \\
+ \iint_{\Omega_2} (\nabla \cdot \tilde{\boldsymbol{u}}) \bar{p}^{n+1} \, \mathrm{d}\boldsymbol{x} + \iint_{\Omega_2} \rho\big(h^n, p_0(t^n)\big) \boldsymbol{g} \cdot \tilde{\boldsymbol{u}} \, \mathrm{d}\boldsymbol{x}, " \quad (11c)
\end{aligned}$$

where

$$\mathrm{H} = \{h \in \mathrm{H}^1(\Omega_2),\ h(x,0) = 0\} \text{ and } \mathrm{U} = \{\boldsymbol{u} \in \mathrm{H}^1(\Omega_2)^2,\ \boldsymbol{u}(x,0) = \boldsymbol{0},\ u(0,y) = u(L_x,y) = 0\}.$$

Similarly to the 1D section, $\boldsymbol{\xi}^n$ denotes the foot of the characteristic curve, *i.e.* $\boldsymbol{\xi}^n(\boldsymbol{x}) = \boldsymbol{\chi}(t^n; t^{n+1}, \boldsymbol{x})$ where $\boldsymbol{\chi}$ is the solution to the 2D counterpart of ODE (8).

Jumps involved in (11) enable to account for eventual discontinuities. Within pure phases solutions are expected to be smooth as shown in dimension 1 but jumps may occur with phase transition.

To improve the accuracy of the results, we refine the mesh (using the `isoline` package in FreeFem++) in the mixture and vapour phases where corresponding domains can be small (bubbles).

p_0	Thermodynamic pressure	$155 \times 10^5\,\mathrm{Pa}$ (constant)
μ_0	Dynamic viscosity	$8.4 \times 10^{-5}\,\mathrm{kg \cdot m^{-1} \cdot s^{-1}}$ (constant)
Φ	Power density	$800\Phi_0 \exp\left(\frac{-1}{r^2-\lvert\boldsymbol{x}\rvert^2}\right) \mathbf{1}_{\{\lvert\boldsymbol{x}\rvert \leq r\}}$
ρ_e	Input density	$750\,\mathrm{kg \cdot m^{-3}}$ (constant)
$\boldsymbol{u}_e$	Input velocity	$(0, v_e)$ with $v_e = 1.3\,\mathrm{m \cdot s^{-1}}$ (constant)
h_0	Initial enthalpy	h_e (constant)
$\boldsymbol{u}_0$	Initial velocity	$(0, v_e)$ (constant)

Table 2: Parameters for 2D simulations

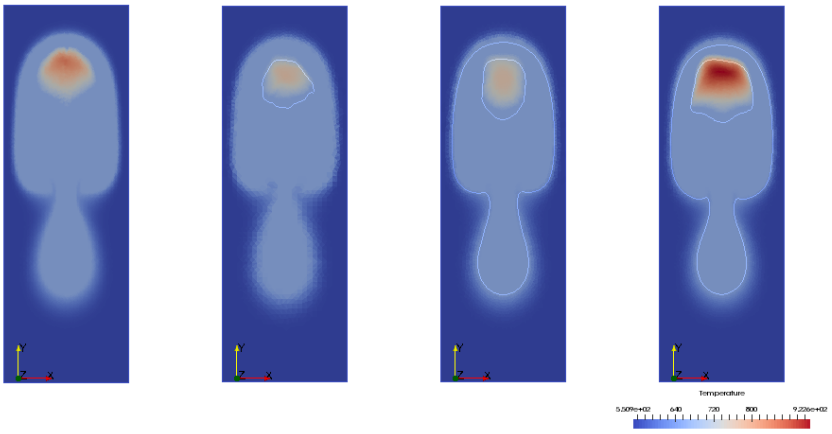

Figure 6: Temperature at time $t = 0.59\,\mathrm{s}$. From left to right: reference test case with a fine mesh (100×300); 25×75 with 4-time refinement in the vapor phase; 25×75 with 2-time refinement in the mixture phase and 4-time refinement in the vapor phase; 25×75 with 3-time refinement in the mixture phase and 6-time refinement in the vapor phase. White lines correspond to the level sets of h between phases.

3.2 Numerical results

We take $L_x = 1\,\mathrm{m}$ and $L_y = 3\,\mathrm{m}$. Φ_0 is the value reported in Table 1(b). We consider here an overestimated power density to make vapour appear. It is compactly supported with a disk of radius $r = 0.5$.

Due to strong variations of the velocity field when passing from one phase to another, a classical hyperbolic CFL condition for the time step is necessary rather than an arbitrary threshold. As stated before, to capture accurately the surfaces where phase change occurs, a refinement procedure is run in mixture and vapour phases. The results are analysed from two points of view: we focus first on the accuracy and the computational efficiency and then on the influence of the thermal conductivity to confirm preliminary results in 1D.

3.2.1 Accuracy issues

Due to the specifications of FreeFem++, mesh definitions are parametrised by the number of nodes on each boundary. For the accuracy investigation, we consider:

- A fine mesh corresponding to 100 nodes on horizontal boundaries (top and bottom) and 300 nodes on vertical boundaries (lateral walls);

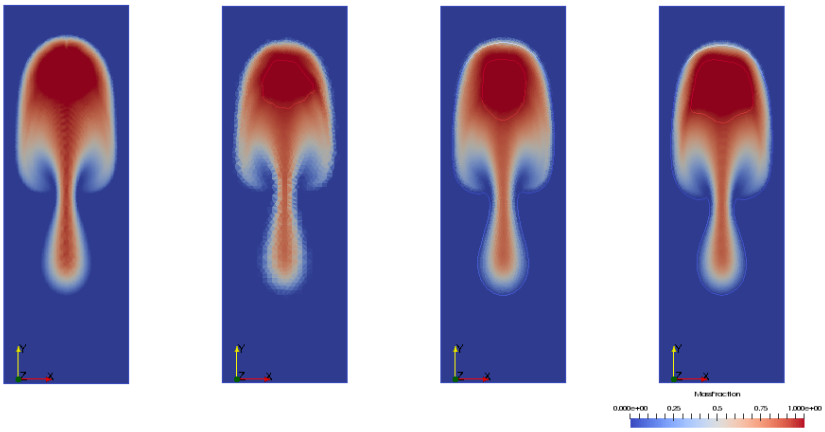

Figure 7: Mass fraction at time $t = 0.59\,\mathrm{s}$. From left to right: reference test case with a fine mesh (100×300); 25×75 with 4-time refinement in the vapor phase; 25×75 with 2-time refinement in the mixture phase and 4-time refinement in the vapor phase; 25×75 with 3-time refinement in the mixture phase and 6-time refinement in the vapor phase. White lines correspond to the level sets of h between phases.

- Coarser meshes based on a 25 horizontal / 75 vertical nodes with different rates of refinement in mixture and vapour phases (see legends of Figures 6-7).

We can observe on the temperature representations (Fig. 6) the level sets $h = h_{\mathfrak{l}}^s$ and $h = h_{\mathfrak{g}}^s$ depicted with white lines separating phases. At the selected time (0.59 s) the three phases are present and we recover a constant temperature (equal to T^s) in the whole mixture domain. We also remark that the finer the mesh, the wider the vapour domain. The figure on the far right (finest refinement) seems even more accurate than the one on the far left (finest mesh) while it comprises fewer nodes. From a computational point of view, it runs 5-time faster than the fine case. Hence the refinement strategy turns out to be relevant in the balance accuracy/efficiency.

Figure 7 represents the mass fraction on the different meshes. We can observe the Rayleigh-Taylor instability due to the gravity field: the water is flowing upwards while the gravity is pointing downwards. The density decreases as the enthalpy increases which makes the mixture lighter than the liquid. The lighter phase is then sped up through the heavier phase above which induces the instability. The shapes are the same no matter what the mesh and the front evolves at the same velocity. The very difference lies in the domain occupied by vapour which is wider in the right case.

3.2.2 Influence of the thermal conductivity

We investigate here the influence of the taking into account of the thermal conduction terms. We run the non-diffusive algorithm designed in [5] and the diffusive version described above (§ 3.1) over the same fine mesh with 100 horizontal / 300 vertical nodes. The computational times are almost the same. The conductivity is set to standard physical values ($\lambda_{\mathfrak{l}} = 0.6$ and $\lambda_{\mathfrak{g}} = 0.08$).

We see on Figure 8 that it is hard to distinguish the numerical solutions (enthalpy variable) for $\Lambda = 0$ and $\Lambda \neq 0$. The cross-section in the middle of the core (on the right) shows that the only noticeable discrepancy occurs in the mixture phase. Hence these 2D results lead to the same conclusion as previous 1D results: in conditions close to those in a PWR core – nominal or accidental, the thermal conductivity does not imply major changes in the solution of the Lmnc-model. This legitimates not to take it into account in future works.

We finally mention two facts: on the one hand, results do not exhibit jumps for the variables of interest while the study in 1D raises issues when vapour appears. On the other hand, while a DG method was

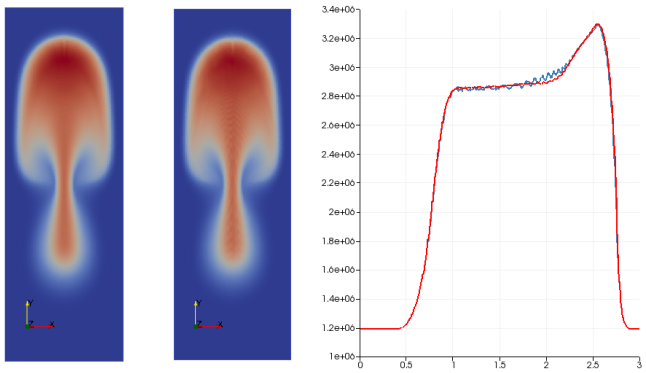

Figure 8: Enthalpy at time $t = 0.59\,\mathrm{s}$ on a fine mesh (100×300). Left: LMNC-model with $\lambda = 0$. Right: LMNC-model with $\lambda_\mathfrak{l} = 0.6$ and $\lambda_\mathfrak{g} = 0.08$. The graph represents the values of the enthalpy on the vertical line ($x = L_x/2, 0 \leq y \leq L_y$): in red for the non-diffusive solution and in blue for the diffusive one.

applied to the standard formulation of the LMNC-model, another strategy was carried out in [6], namely an equivalent reformulation of the equations: the term between brackets in the right hand side of (1a) is replaced using Equation (1b) so that a standard Lagrange FE method can be applied. However, we do not state that any of these methods is proven to be more efficient.

4 Conclusion

The present work consisted in taking into account additional physical phenomena in the modelling of fluid flows in nuclear reactor cores by means of the LMNC-model. On the one hand, thermal conduction effects induce a change in the mathematical structure of the equations and significant adaptations of the numerical schemes. But we managed to handle it in the 1D MOC scheme by solving directy the implicit version of the diffusive scheme and in the 2D scheme using features of the FREEFEM++ software. We even improved the accuracy of the 2D algorithm by means of a refinement strategy. On the other hand, considering a (given) time-varying thermodynamic pressure raises no particular issues from the computational point of view but may increase the computational time when fitting tabulated values for the equation of state.

The conclusion of the numerous simulations run in this paper is that the resulting numerical methods are robust to these modifications. They showed that the thermal conductivity does not play a major role in nominal or accidental conditions of a PWR core which enables to leave it apart in future works. The new algorithms are now able to deal with more complex configurations like depressurisation processes for safety evaluations. The LMNC tools are improved step by step to provide reliable results for nuclear engineering. Next perspectives will concern extensions to a 3D robust code and the coupling with neutronics to better model the power density [7]. Applications to other types of reactors may also be contemplated.

Acknowledgements

The project DIPLOMA on the occasion of the 2015 CEMRACS was funded by the CNRS project call "NEEDS" (nuclear, energy, environment, waste and society) for which CDMATH was selected in 2014 and 2015.

References

[1] W.F. Ames. *Numerical methods for partial differential equations*. Academic press, 1977.

[2] M. Bernard, S. Dellacherie, G. Faccanoni, B. Grec, O. Lafitte, T.-T. Nguyen, and Y. Penel. Study of low Mach nuclear core model for single-phase flow. In *ESAIM:Proc*, volume 38, pages 118–134, 2012.

[3] M. Bernard, S. Dellacherie, G. Faccanoni, B. Grec, and Y. Penel. Study of a low Mach nuclear core model for two-phase flows with phase transition I: stiffened gas law. *Math. Model. Numer. Anal.*, 48(6):1639–1679, 2014.

[4] S. Dellacherie. On a low Mach nuclear core model. In *ESAIM:Proc*, volume 35, pages 79–106, 2012.

[5] S. Dellacherie, G. Faccanoni, B. Grec, E. Nayir, and Y. Penel. 2D numerical simulation of a low Mach nuclear core model with stiffened gas using FreeFem++. In *ESAIM:ProcS*, volume 45, pages 138–147, 2014.

[6] S. Dellacherie, G. Faccanoni, B. Grec, and Y. Penel. Study of a low Mach nuclear core model for two-phase flows with phase transition II: tabulated equation of state. 2016.

[7] S. Dellacherie and O. Lafitte. Une solution explicite monodimensionnelle d'un modèle simplifié de couplage stationnaire thermohydraulique-neutronique. 2016.

[8] P. Embid. Well-Posedness of the nonlinear Equations for zero Mach Number Combustion. *Communications in Partial Differential Equations*, 12(11):1227–1283, 1987.

[9] J.M. Gonzalez-Santalo and R.T. Jr Lahey. An exact solution for flow transients in two-phase systems by the method of characteristics. *J. Heat Transf.*, 95(4):470–476, 1973.

[10] F. Hecht. New development in FreeFem++. *J. Numer. Math.*, 20(3-4):251–266, 2012.

[11] S. Klainerman and A. Majda. Compressible and incompressible flows. *Comm. Pure Appli. Math.*, 35:629–651, 1982.

[12] R. Klein. Semi-implicit extension of a Godunov-type scheme based on low Mach number asymptotics I: One-dimensional flow. *J. Comput. Phys.*, 121(2):213–237, 1995.

[13] E.W. Lemmon, M.O. McLinden, and D.G. Friend. *Thermophysical Properties of Fluid Systems*. National Institute of Standards and Technology, Gaithersburg MD, 20899.

[14] A. Majda and J. Sethian. The derivation and numerical solution of the equations for zero Mach number combustion. *Combust. Sci. Technol.*, 42(3-4):185–205, 1985.

[15] Y. Penel. An explicit stable numerical scheme for the 1d transport equation. *Discrete Contin. Dyn. Syst. Ser. S*, 5(3):641–656, 2012.

[16] Y. Penel, S. Dellacherie, and B. Després. Coupling strategies for compressible – low Mach number flows. *Math. Models Methods Appl. Sci.*, 25(6):1045, 2015.

[17] O. Pironneau. On the transport-diffusion algorithm and its applications to the navier-stokes equations. *Numer. Math.*, 38:309–332, 1982.